NANO LETTERS

Letter

Dendrimer-Au Nanoparticle Network Covered Alumina Membrane for Ion Rectification and Enhanced Bioanalysis

Chen Wang,* Xiao-Ping Zhao, Fei-Fei Liu, Yuming Chen, Xing-Hua Xia,* and Ju Li*

Cite This: Nano Lett. 2020, 20, 1846−1854

Read Online

ACCESS | Metrics & More | Article Recommendations | SI Supporting Information

ABSTRACT: Ion transport in an artificial asymmetric nanoporous membrane, which is similar to biological ion channels, can be used for biosensing. Here, a dendrimer-Au nanoparticle network (DAN) is *in situ* assembled on a nanoporous anodic aluminum oxide (AAO) surface, forming a DAN/AAO hybrid membrane. Benefiting from the high surface area and anion selectivity of DAN, the prepared DAN/AAO hybrid presents selective ion transport. Under a bias potential, a diode-like current−potential (I−V) response is observed. The obtained ionic current rectification (ICR) property can be tuned by the ion valence and pH value of the electrolyte. The rectified ionic current endows the as-prepared DAN/AAO hybrid with the ability of enhanced bioanalysis. Sensitive capture and detection of circulating tumor cells (CTCs) with a detection limit of 80 cells mL^{-1} as well as excellent reusability can be achieved.

KEYWORDS: dendrimer-Au nanoparticle network, hybrid membrane, ion selectivity, ionic current rectification, enhanced bioanalysis
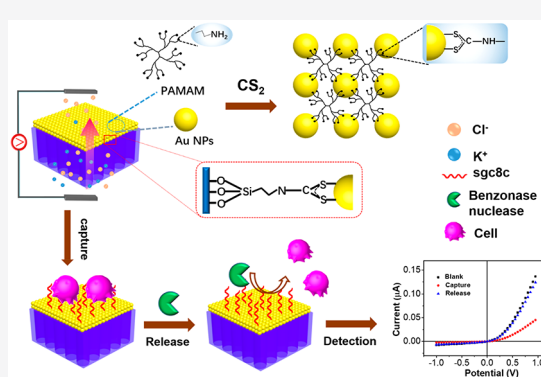
Ionic current rectification (ICR) is seen in biological or artificial nanochannels,[1−4] where a nonlinear and asymmetric current−potential (I−V) curve appears due to asymmetric ionic transport. Generally, ICR can occur in the cases of symmetry breaking in the structure, surface charge distribution, bulk electrolyte concentration, or combinations of these factors.[5−7] The correlation between ICR properties and the degree of symmetry breaking was precisely demonstrated, taking the DNA-stuffed nanochannel as the model system.[4] Up to now, a variety of techniques have been developed for the fabrication of ICR devices such as direct modification, plasma grafting, and ion sputtering,[8−16] in nanofluidic devices including nanopores with an asymmetric geometry,[8,9] homogeneous nanochannels with asymmetric surface modifications,[10,11] hybrids composed of varied nanomaterials,[12−14] and dynamic curvature nanochannels.[15] For example, by laminating the polystyrene-*b*-poly(4-vinylpyridine) membrane and polyethylene terephthalate membrane, a heterogeneous polymer membrane displaying a highly ICR characteristic was constructed.[16] Recently, some inert or conductive nanochannels/nanopores have been directly fabricated on thin metal films, on which detection of nanoparticles,[17,18] biomolecules,[19] or asymmetric ionic transport[20] have been successfully performed.

The network formed by functional nanomaterials and ligands provides a simple, robust, and highly efficient fabrication technique for the construction of novel nanoporous structures.[21−24] Compared to traditional solid nanoporous materials, the network has a more exposed surface area. For example, by grafting gold spheres on a glass nanopipette with

the DNA linker, a pH-responsive structure was successfully fabricated.[24] Owing to the tunable distance within Au nanoparticles (AuNPs) by the DNA linker, the fabricated nanodevice presents varied ICR properties under different pH values. The nonuniform geometry and surface charge density endow the formed device with tunable ICR properties. These interesting works provide new strategies to design and develop multifunctional heterogeneous hybrid devices with a high ICR response for seawater desalination,[13] energy conversion,[16] and bioanalysis/sensors.[8,9]

Sensitive and selective cell capture and detection play important roles in the prognosis and treatment of cancer.[25] Recently, we developed a nanochannel−ion channel hybrid with an ICR property for the efficient capture and detection of circulating tumor cells (CTCs).[26] Due to the unique ICR characteristic, the CTC concentrations ranging from 1×10^2 to 2×10^6 cells mL^{-1} can be successfully detected with a detection limit of 100 cells mL^{-1}. However, in that work, only the outer surface of the anodic aluminum oxide (AAO) membrane can be used. The fewer surface areas, as well as a relatively smooth surface, is a big challenge for efficient cell capture. In addition, the ion channel dimensions are fixed, and cannot be tuned flexibly. The super small size of the ion
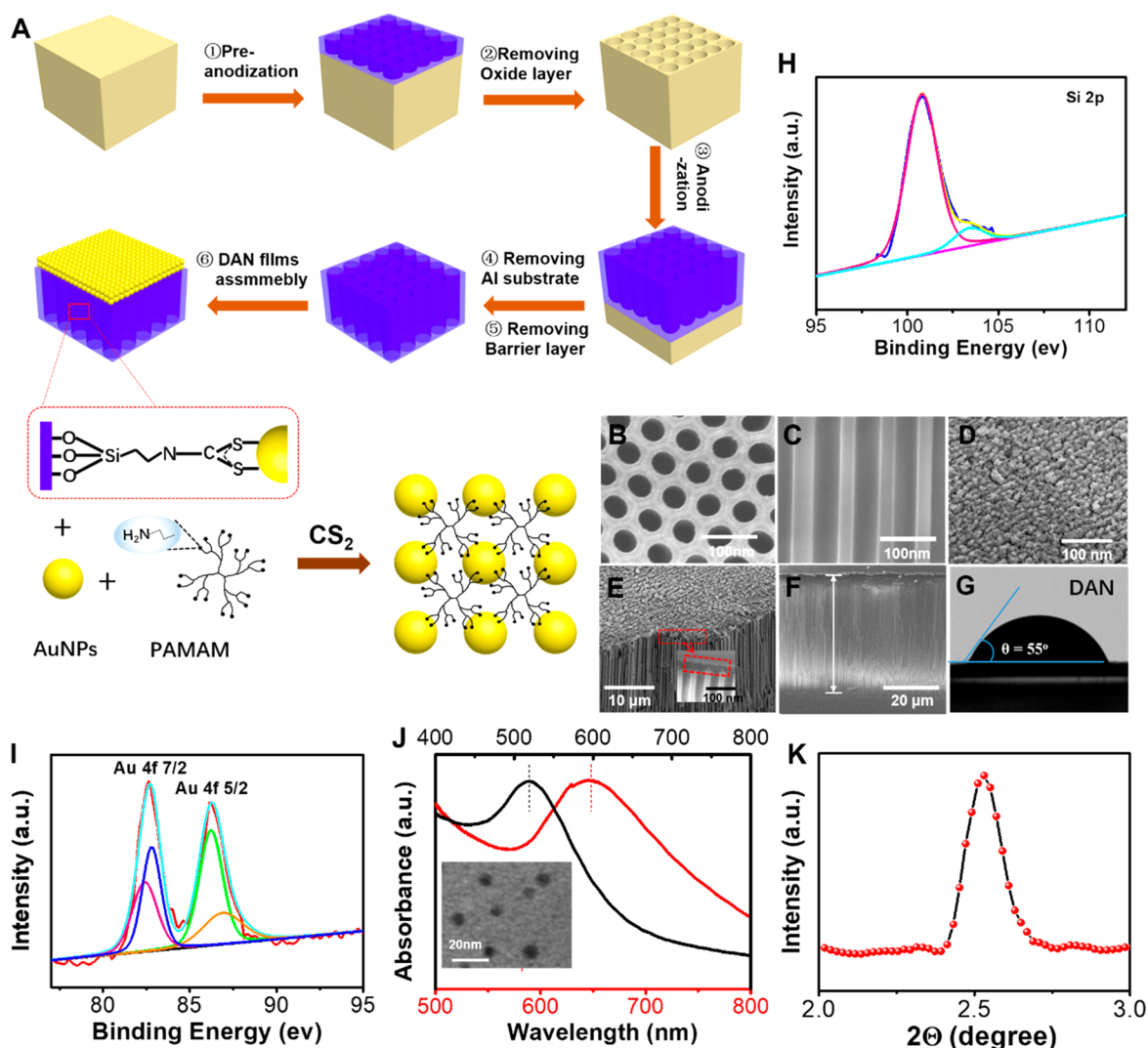
Figure 1. (A) Schematic illustration of the preparation of the DAN/AAO hybrid. (B−F) SEM images of the DAN/AAO hybrid. (B) Top of the DAN/AAO hybrid. (C) Cross section of AAO. (D) DAN film. (E) Cross section of the DAN/AAO hybrid. The inset is the enlarged image of the cross section. (F) The thickness of the whole DAN/AAO hybrid. (G) The contact angle of the DAN film. (H−I) XPS spectra of the DAN/AAO hybrid ((H) XPS curve of APTES; (I) XPS curve of AuNPs). (J) UV−vis spectra of the prepared AuNPs and DAN film. Black curve: pure AuNPs solution. Red curve: AuNPs containing the PAMAM dendrimer and CS_2 solution. The inset shows the TEM image of the prepared AuNPs; the scale bar is 20 nm. (K) SAXRD patterns for the DAN composites.

channels may prevent the relatively bigger drug molecules or negatively charged molecules from passing through, which will limit its applications in cell downstream analysis, such as drug transport, screening, and cancer therapy.

Herein, we reported a new ionic rectification device fabricated by assembling the AuNPs network on the surface of the AAO membrane for CTCs analysis. Dendrimer (poly(amidoamine) (PAMAM)) and carbon disulfide (CS_2) were used as the linkers to connect AuNPs, forming a dendrimer−nanoparticle network (denoted as DAN in the following work) film. This cross-linked DAN film can be *in situ* assembled onto the surface of AAO by chemical coupling of the −N−C bond in DAN with amine-functionalized AAO, forming the DAN/AAO hybrid. The high surface-to-volume ratio, as well as exposed functional groups on the DAN film, will provide abundant active sites for molecular anchoring, which is of critical importance to efficient and selective cell capture. The symmetry breaking by covering DAN on one side of AAO endows the hybrid with an excellent ICR property,

ensuring highly sensitive cell detection. Finally, the captured cells can be released with nearly no damage under the action of benzonase, endowing the hybrid with the ability to be reused with excellent durability. Therefore, the present DAN/AAO hybrid is expected to behave as a robust and sensitive biosensor toward cell analysis and detection. Besides, the AuNPs in DAN film possesses an unique localized surface plasmon resonance (LSPR) characteristic that would enable highly accurate characterizations such as surface-enhanced Raman scattering (SERS)[27] and electrochemistry[28] and open an avenue for combining fluidics with plasmonics.

◼ RESULTS AND DISCUSSION

Fabrication and Characterization of the DAN/AAO Hybrid. The fabrication process is illustrated in Figure 1A. AAO was prepared using the method described previously.[29] To obtain the amine-functionalized AAO, AAO was immersed into a 1% (3-aminopropyl) triethoxysilane (APTES) solution for 12 h, followed by rinsing with ethanol and drying in
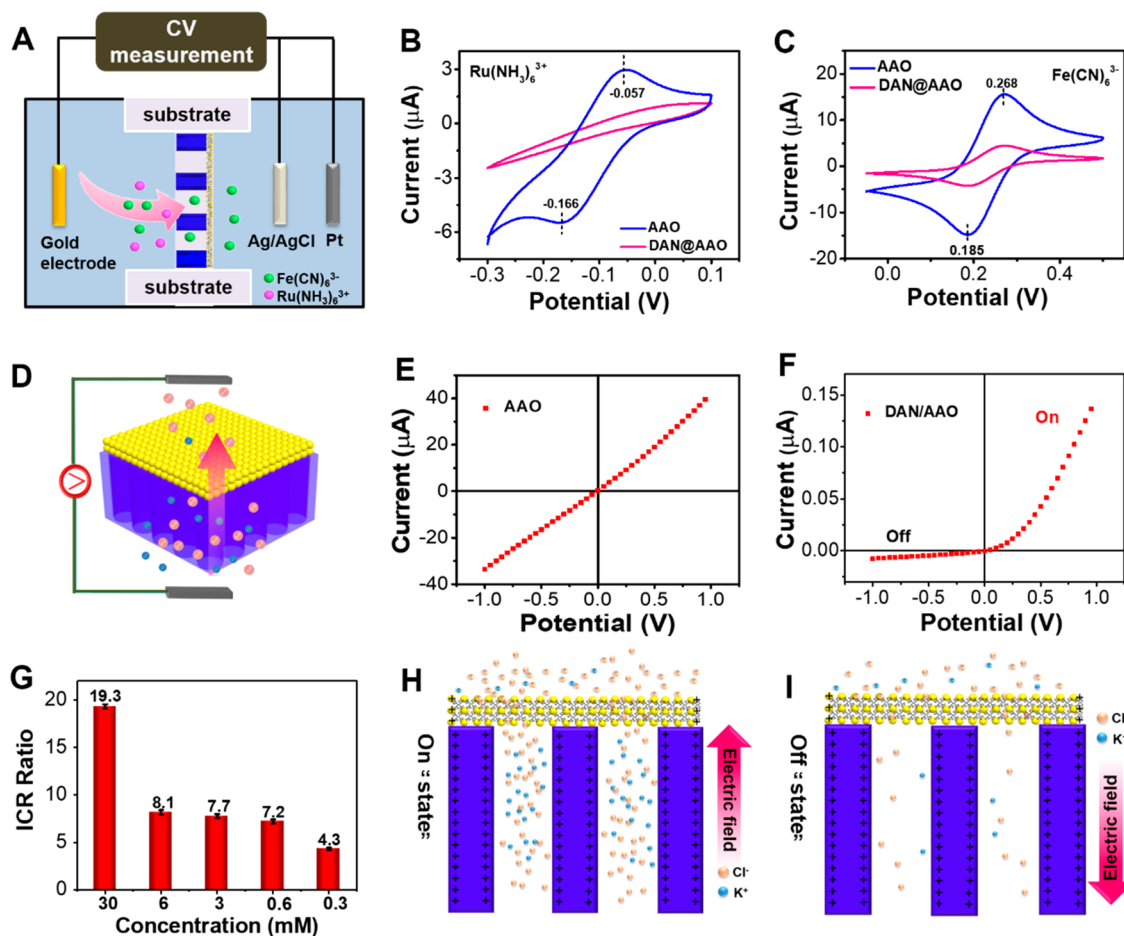
Figure 2. (A) Setup for CV measurements. The substrate in the figure is used to fix the DAN/AAO hybrid. CVs of the DAN/AAO hybrid (red curve) and bare AAO (blue curve) electrode in 1 mM KCl containing 0.5 mM $Ru(NH_3)_6^{3+}$ (B) and $Fe(CN)_6^{3-}$(C). The scan rate was 50 mV s^{-1}. (D) Schematic illustration of the setup for the measurement of $I-V$ curves. (E) $I-V$ curve of AAO in 1 mM KCl at pH 7.0. (F) $I-V$ curve of the DAN/AAO hybrid in 1 mM KCl at pH 7.0. (G) Rectification ratio of the DAN/AAO hybrid at different AuNP concentrations (30 mM, 6 mM, 3 mM, 0.6 mM, 0.3 mM). (H, I) Illustration of the ICR mechanism of the DAN/AAO hybrid.

nitrogen gas. The prepared amine-functionalized AAO was then placed at the bottom of a small vial containing a mixture consisting of 4-dimethylaminopyridine (DMAP) stabilized AuNPs (∼7 nm),[30] CS_2 methanol solution, and PAMAM dendrimer methanol solution. The gold nanoparticles were assembled on the top surface of AAO linked by CS_2, forming the DAN film. Following the completion of the reaction, the remaining solution was removed, and the DAN/AAO hybrid was obtained.

To characterize the morphology of the fabricated AAO, scanning electron microscopy (SEM) was used. Figure 1B–E indicates the successful formation of the DAN/AAO hybrid. The fabricated AAO has regular pores of ∼40 nm in diameter (Figure 1B,C). The upper layer of AAO was covered by the DAN film (Figure 1D,E). The thickness of the DAN film is around 40 nm (inset of Figure 1E). The entire thickness of the DAN/AAO hybrid is ∼50 μm (Figure 1F). The contact angle on both sides of the hybrid was measured (Figure 1G and Figure S1), indicating the hydrophilicity of the DAN film and the hybrid. High-resolution spectra of X-ray photoelectron spectroscopy (XPS) was used to further prove the successful assembly of DAN. It is notable that the DAN/AAO hybrid exhibits singular signals at 101.4 eV ascribed to −Si−O− from the coupling reagent of APTES (Figure 1H) and two obvious Au 4f peaks at 82.5 and 86.5 eV, respectively, from AuNPs

(Figure 1I). In addition, energy dispersive spectroscopy (EDS) mapping of the SEM images (Figure S2) was used to identify the elemental distribution of Au, Si, N, O, and C.[31] It can be seen that the Au and Si atoms are dispersed homogeneously in the architecture, indicating the formation of the DAN film on the top of AAO. These results demonstrate the successful formation of the DAN/AAO hybrid.

To verify the formation mechanism of the DAN film, UV−vis spectra were used to examine the interaction between PAMAM and AuNPs. The results are shown in Figure 1K, showing a dominant absorption peak at ∼518 nm (black curve in Figure 1J, an average diameter of 7 ± 1 nm in this work shown in the inset of Figure 1J). This absorption resulted from the characteristic plasmonic absorption of isolated AuNPs. After reaction with CS_2 and the PAMAM dendrimer, the absorption peak shifted to ∼647 nm due to the change in the dielectric environment (red curve in Figure 1J). The results are in accordance with the previous work.[24] The interparticle spacing for the DAN film was determined by the small-angle X-ray diffraction (SAXRD) patterns (Figure 1K) using the Bragg diffraction eq ($2\theta = 2.4$) is less than 4.5 nm.[24] To further confirm the interparticle spacing for the DAN film, AuNPs, PAMAM, and CS_2 were assembled in solution to form the same structure of the DAN film. The TEM image (Figure S3)
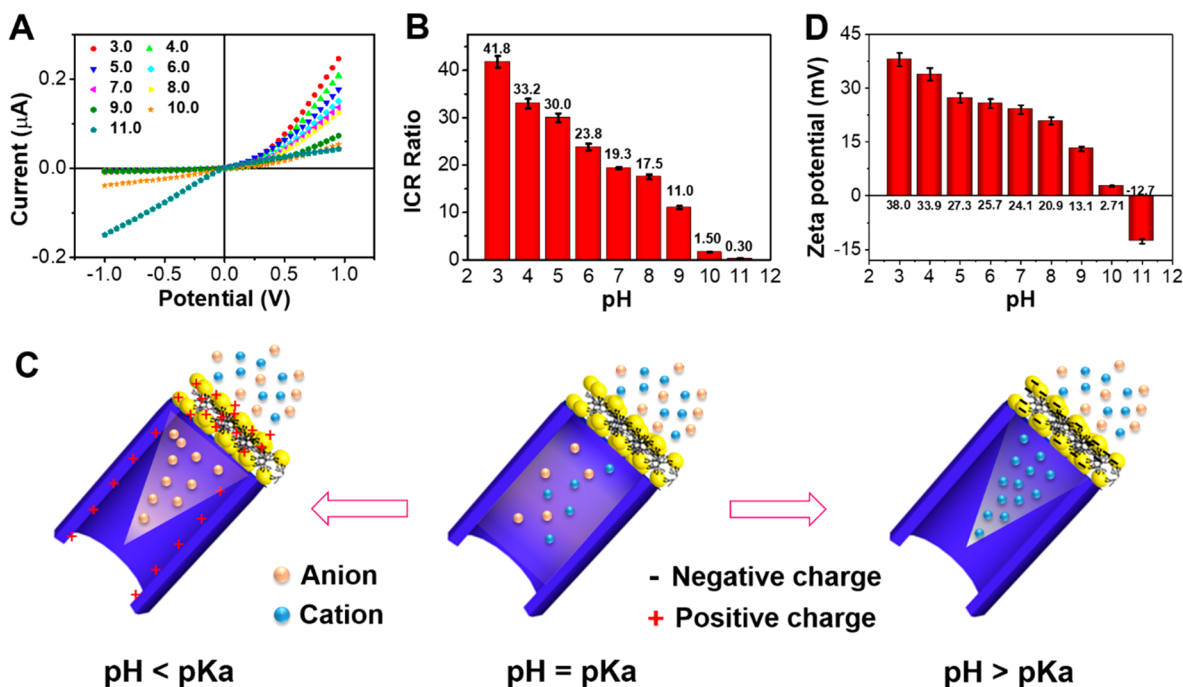
Figure 3. $I-V$ curves measured on the DAN/AAO hybrid in solutions with different pH values. (B) Rectification ratio of the DAN/AAO hybrid in solutions with different pH values. (C) Mechanism of ion transport through the DAN/AAO hybrid in solutions with varied pH values (brown spheres represent anions; blue spheres represent cations). (D) The ζ potential of DAN fragments at different pH values.

shows that the nanopores exist among neighboring AuNPs in the DNP film with the size of interparticle spacing $\sim$ 3.6 nm.

Ion Transport Properties of the DAN/AAO Hybrid. The ion selectivity of the DAN/AAO hybrid was examined by cyclic voltammetry (CV) using Ru $(NH_3)_6^{3+}$ or Fe $(CN)_6^{3-}$ as the electrochemical probes, respectively, in 1 mM KCl aqueous solution. The electrochemical setup is schematically shown in Figure 2A. Then, 0.5 mM Ru $(NH_3)_6^{3+}$ or Fe $(CN)_6^{3-}$ was put into one of the two half cells for CV measurements. Gold, Ag/AgCl, and platinum wire were used as the working electrode, reference electrode, and auxiliary electrode, respectively. Figure 2B,C shows the CVs obtained with bare AAO and the DAN/AAO hybrid. Both $Ru(NH_3)_6^{3+}$ and Fe $(CN)_6^{3-}$ could transport through the bare AAO as evidenced by the obvious redox peaks. In comparison with the bare AAO, the DAN/AAO hybrid film shows anion selective transport properties due to the existence of surface charges since only the redox current for the ferricyanide anion can be observed (Figure 2C). There is no redox current observable for the electrochemical probe of Ru(NH$_3$)$_6^{3+}$ cation (Figure 2B). This suggests DAN is anion-selective, allowing only anions to pass. Because the pK$_a$ of DMAP ligands on the AuNPs surface is 9.6,[30] DAN should be positively charged when the pH is less than 9.6. The interstitial spacing in DAN is less than 4.5 nm, so it interacts very strongly with ions that try to pass through the interstices of the network.

The ionic transport properties of the DAN/AAO hybrid were investigated using two Ag/AgCl electrodes (Figure 2D). For the pure AAO film, an Ohmic linear $I-V$ curve is observed (Figure 2E). After DAN was modified to the AAO surface, the ionic current displays a diode-like $I-V$ curve (Figure 2F) due to the existence of asymmetry in the structure and surface charge density from the linkers. To achieve the high-performance ICR device, the influencing factors including AuNPs concentrations, channel size, and AAO thickness were

investigated. Figure 2G shows the effect of AuNP concentration on ICR (the $I-V$ curves refer to Figure S4). With an increasing AuNP concentration, the ICR ratio ($f \equiv I_{+1\,V}/I_{-1\,V}$, $I_{+1\,V}$ is denoted as the current value at +1.0 V, $I_{-1\,V}$ is denoted as the absolute current value at −1.0 V) significantly increases to a maximum value of 19.3 when the film was prepared with 30 mM AuNPs. It has been reported that decreasing the density of dendrimers between particles will decrease the interparticle spacing.[32] To keep the same quantity of dendrimers, an increased AuNPs concentration will decrease the ratio of dendrimers in the DAN layer, resulting in a smaller interparticle spacing in the DAN film. The ion transport is influenced by both ion selectivity and ion conductivity. The ion conductivity of the hybrid will decrease as the interparticle spacing in the DAN film gets smaller, resulting in a decrease of ionic current (Figure S4). However, the ICR property was determined by the distinct transport actions of co-ions and counterions in the nanochannels.[10,33] The decreased channel size will contribute to more excellent ion selectivity. Thus, a higher ICR ratio can be expected in the case of a smaller interparticle spacing in the DAN film. The effects of the AAO channel size and thickness (Figure S5 and Figure S6) indicate that the channel size could influence the ICR property efficiently, while AAO thickness does not. The effect of surface charges will be weakened with the increase of channel size, which in turn decreases the ICR efficiency. Interestingly, although there is little influence of the AAO thickness on the dimensionless ICR ratio, it was found that the ionic current decreases slightly as AAO becomes thicker (Figure S6A), caused by the increased electric resistance for thicker AAO. Considering all factors in the fabrication and device performance, the DAN/AAO hybrid prepared by 30 mM AuNPs and AAO with a 40 nm diameter was used in the following measurements.
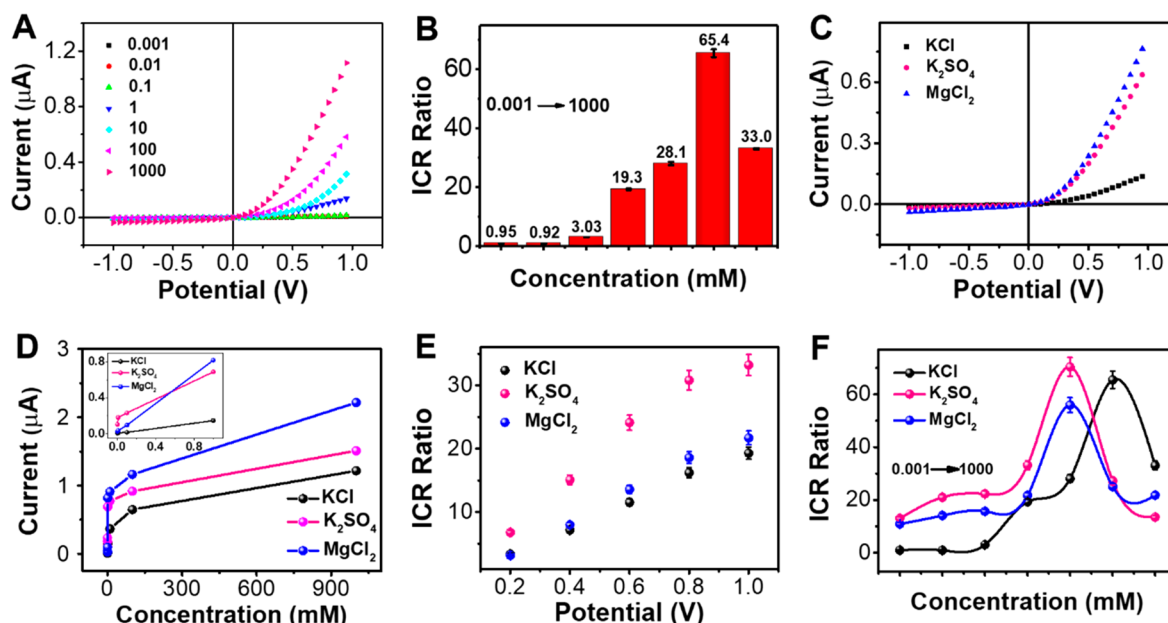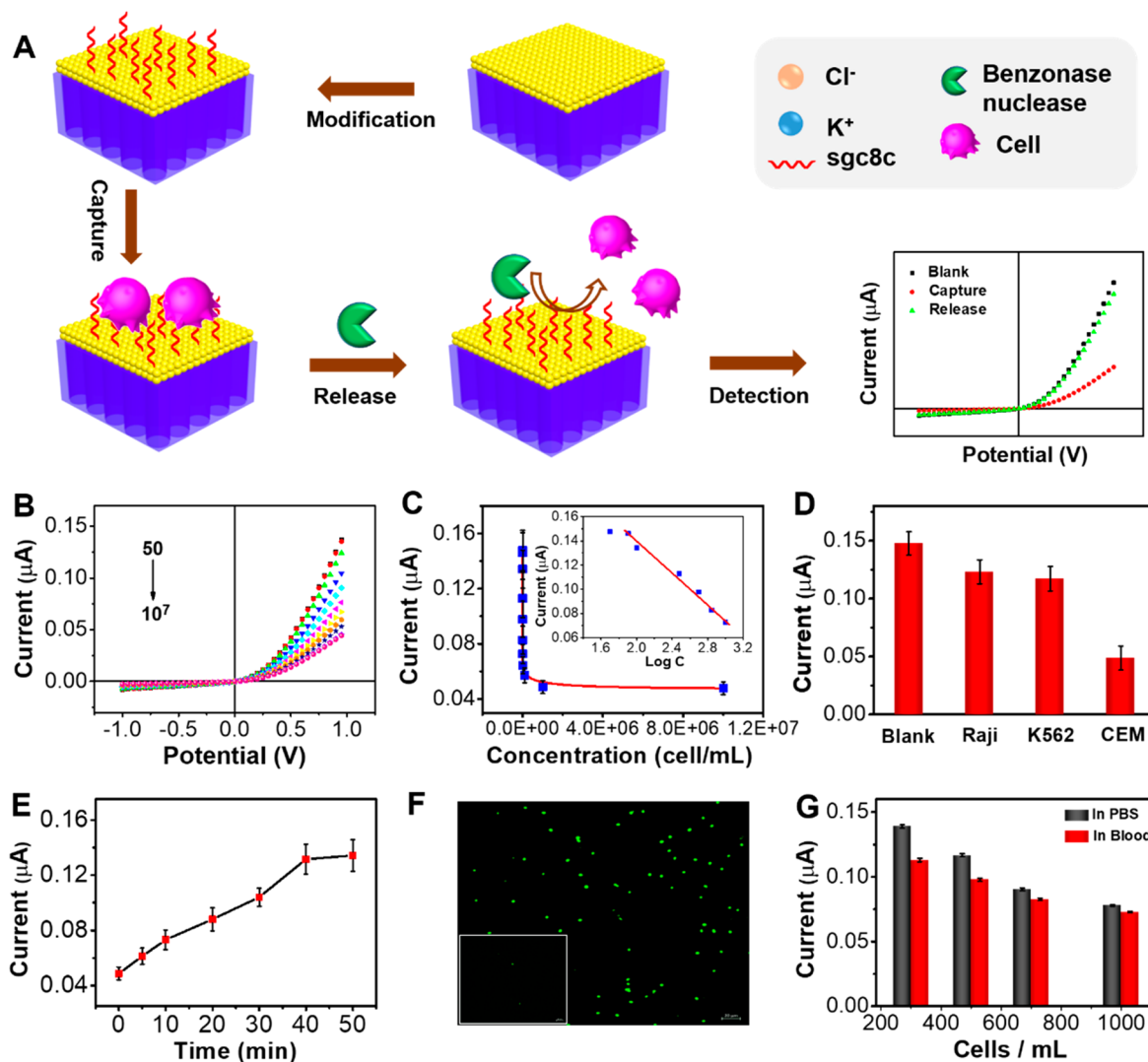
Figure 4. (A) $I-V$ curves of the DAN/AAO hybrid at different concentrations of KCl. (B) Rectification ratio of the DAN/AAO hybrid at different concentrations of KCl. (C) $I-V$ curves of the DAN/AAO hybrid at different electrolytes (KCl, K_2SO_4, and $MgCl_2$) with the same concentration in 1 mM. (D) Current value at +1.0 V at different electrolytea (KCl, K_2SO_4, and $MgCl_2$) with different concentrations. The inset was the enlargement of panel D at a low concentration. (E) Rectification ratio of the DAN/AAO hybrid at different electrolytes (KCl, K_2SO_4, and $MgCl_2$) with the same concentration in 1 mM at a potential from +0.2 V to +1.0 V. (F) Rectification ratio with different electrolytes under different concentrations.

The ICR mechanism of the present hybrid is schematically shown in Figure 2H,I. While the pK_a of pure AAO is around 6, the pK_a of the primary amine group of the PAMAM dendrimer and APTES is around 10.0,[34] so we expect our amine-functionalized AAO to be positively charged when the pH value is less than 10.0. Under a pH = 7 environment, therefore, both DAN and AAO should be positively charged. When the electric field is applied from the bottom (AAO) side to the top (DAN) side, cations (K^+) are driven from bottom to top, and anions (Cl^-) from top to bottom. While Cl^- can freely pass the anion-selective DAN, K^+ would be stopped by the DAN and accumulate inside the AAO nanochannel. To maintain electroneutrality, some Cl^- would stay to accompany K^+, increasing the ionic strength. The increased ion concentration within the AAO nanochannel results in a reduced electrical double layer (EDL) thickness, and so more Cl^- can pass through the hybrid, unencumbered by the charge on amine-functionalized AAO. We called this the "on" state (Figure 2H). In comparison, when the electric field is applied from the top (DAN) side to the bottom (AAO) side, the cations (K^+) are driven from top to bottom, which, however, will be excluded by DAN because it is anion-selective. Also, those K^+ previously stored inside the nanochannel will be driven out and exit from the bottom. The Cl^- are driven from bottom to top, but they flow through DAN, so they are not accumulated inside the AAO tubule either; therefore, the ions within AAO nano-channels are depleted, resulting in a reduced ionic strength, larger EDL, and decreased Cl^- current. Under the extreme condition, nearly no Cl^- ions flow through the hybrid, and accordingly, the hybrid presents the "off" state (Figure 2I).

Effect of pH on Ion Transport. The pH value has a significant influence on the ion transport behavior of the present DAN/AAO hybrid. Figure 3A shows the measured $I-V$ curves of the DAN/AAO hybrid under different pH values. Figure 3B is the rectification ratio calculated from Figure 3A,

which decreases as the pH value changes from 3.0 to 10.0, then rapidly declines to $f < 1$ (reversed ICR direction) at pH 11.0. The pH-tunable ICR property is schematically illustrated in Figure 3C. As has been described above, the present hybrid is positively charged when the pH value is less than 10.0. At a lower pH, the DAN/AAO hybrid surface will carry more positive charges that attract more anions passing through the DAN/AAO hybrid. Thus, a higher ICR property can be expected. With increasing the pH value to 10.0, the ionic current and ICR ratio decrease due to the declined positive surface charge. It is furthermore observed that the $I-V$ property of the DAN/AAO hybrid sustains reversion at pH 11.0 ($f = 0.3$). The amino groups are neutral at a high pH,[15] but the acylamion groups from PAMAM may partially hydrolyze at a high pH value (pH 11.0) because the pK_a of acylamion groups is around 10.0.[35] Therefore, the surface of AAO nanochannels is neutral, but the DAN film might be negatively charged in this condition. The ionic current will be dominated by cations (K^+) rather than Cl^- ions. Under this circumstance, the $I-V$ properties of the DAN/AAO hybrid is reversed: a high conducting ("on") state for $V < 0$ and a low conducting ("off") state for $V > 0$. When the solution pH is equal to pK_a, the hybrid is electroneutral, and thus nearly no ICR will be observed. To keep a constant pH value, the effect of temperature on the mass transport property of the hybrid was also investigated (Figure S7). The currents of both "on" and "off" states increase as the temperature increases. However, the current of the "on" state increases more significantly than that in the "off" state, resulting in an increased ICR ratio at a higher temperature. This result is in accordance with previous work.[36]

To further quantify the charge change at different pH, the ζ potential of the self-assembled DAN fragments was determined by mixing AuNPs, CS_2, and PAMAM dendrimer. As shown in Figure 3D, the measured ζ potentials changed from 38.0 mV to

Figure 5. (A) Schematic demonstration of the CTCs capture and release processes and the corresponding $I-V$ curves of the DAN/AAO hybrid. (B) $I-V$ properties of the DAN/AAO hybrid after capturing different concentrations of CCRF-CEM cells (50, 80, 100, 300, 500, 700, 1000, 10^4, 10^5, 10^6, and 10^7 cells mL^{-1}). (C) Currents at +1.0 V vs CCRF-CEM cell concentration. Inset: the linear calibration plot of the changed current value vs the logarithm of cell concentrations at cell concentrations from 50 to 1000 cells mL^{-1}. (D) Ionic currents at +1.0 V after the capture of different cells. (E) Ionic currents at +1.0 V vs enzyme incubation time. (F) Fluorescence microscopic images of the captured CCRF-CEM cells on the DAN/AAO hybrid, stained by PI/AO. The inset is the fluorescence microscope image of the DAN/AAO hybrid after cells were released. (G) Detection of CTCs in different samples. Results are obtained from PBS buffer and human blood samples, respectively.

2.71 mV, indicating a decreased positive charge density from pH 3.0 to pH 10.0. As expected, the ζ potential changes to −12.7 mV at pH 11.0. The results demonstrate that the solution pH can regulate the surface charges of the DAN/AAO hybrid via protonization/deprotonization, which regulates the ICR properties.

Effect of Ions Concentration and Valence. To further illustrate the ionic transport properties of the DAN/AAO hybrid, different electrolyte concentrations at pH 7.0 were added into two half cells. As shown in Figure 4A, the DAN/AAO hybrid shows different rectified currents for different ion concentrations. The transmembrane current increases with increasing the ion concentration from 0.001 mM to 1 M due to the increased amount of ions through the DAN/AAO hybrid. The ICR ratio (f) increases to 65.4 at 100 mM solution; then, it decreases with further increasing of the ion concentrations (Figure 4B). It is clear the ICR ratio reaches a maximum value when the surface charges are balanced by the counterions in

the EDL.[37] Note that the thickness of electrical double layers is affiliated with the ionic Debye length, λ_D, with $\lambda_D \propto 1/(c_b)^{1/2}$, where c_b is the bulk ionic concentration.[38] Therefore, upon increasing the ionic strength to 1 M, the thickness of EDL decreased, suggesting the decrease of ionic selectivity due to the decline of the EDL screening effect, and thus, the ICR ratio declines. For a system with lower electrolyte concentrations, although the EDL overlapping occurs, the ICR decreases due to fewer ions transported across the channel,[37,39] thus leading to a decline of f.

The valence is another important factor affecting the ion transport characteristics in nanofluidics because it is directly related to the charge inversion process.[40] In this study, the $I-V$ curves of the DAN/AAO hybrid with different valence counterions were measured under different ion concentrations (Figure 4C,D). As shown in Figure 4C, the ion current displays $I(MgCl_2) > I(KCl)$, $I(K_2SO_4) > I(KCl)$, regardless of the applied potential bias. This phenomenon may correlate with

two parameters in principle.[40] The first one is ion concentration, which is higher for the divalent salt at a constant concentration. The second possible factor could correspond to the charge of the ions. Figure 4E illustrates that the largest ICR ratio of the DAN/AAO hybrid is obtained in a 1 mM K_2SO_4 solution regardless of the applied potential bias due to the anion-selective hybrid membrane. Figure 4F demonstrates that f has a local maximum (f_{max}) with varying salt concentrations. In our study, the f_{max} of KCl and K_2SO_4 is achieved at 100 mM and 10 mM, respectively. It is reported that the f could reach its maximum value when the charge on the surface of the DAN/AAO hybrid is balanced by counterions in the EDL.[37] For the DAN/AAO hybrid, the inner surface of DAN/AAO exhibits a positive charge from the amino group at pH 7.0. Since the sulfate ion carries charges as high as twice of the chloride ion, the shielding effect will be stronger in the former case. Consequently, the f of the former reaches the maximum value at a lower electrolyte concentration. In a similar way, the electrolyte concentration at which f_{max} occurs shifts to a lower level when the cation valence increases. The f_{max} for the case of $MgCl_2$ occurs at 10 mM. These phenomena have been explained previously.[41] In addition, if two salts have the same total valences, the salt concentration at which f_{max} occurs is the same, but the value of f_{max} depends on ionic diffusivity.[40] For K_2SO_4 (1:2) and $MgCl_2$ (2:1), the salt concentrations at which f_{max} occur are similar (10 mM). However, the value f_{max} for the case of K_2SO_4 (70.3) is larger than the value f_{max} for $MgCl_2$(55.9). As described above, the as-prepared hybrid membrane is anion-selective, and the anions dominate the ICR property. The charge of a sulfate ion is twice as high as a chloride ion. Keeping a similar liquid flowing rate, more negative charges could be transported through the hybrid in the case of sulfate ions, leading to a higher f_{max} for K_2SO_4 than $MgCl_2$. These results demonstrate the important role of ion valence in the charge inversion and high ICR ratio in an asymmetric nanochannel.

Selective Cell Capture, Detection, and Release. In our DAN/AAO concept, while AAO provides structural support,[42] the DAN covering has a large exposed surface area to the external flowing medium and can be biofunctionalized. Au is well-known to be a highly versatile substrate for chemical and biological analyses. The high surface-to-volume ratio and exposed functional groups on the DAN film provide abundant active sites and room for probing molecular anchoring. Therefore, the prepared hybrid is expected to behave as a biosensor. The performance of the fabricated hybrid as a biosensor was then tested including sensitivity, selectivity, and durability. First, the ability of the present hybrid for cell capture and detection was investigated. As shown in Figure 5A, based on previous work,[26,43] the aptamers that could recognize the special protein on CTC membranes are first immobilized on the DAN surface. As the sample flows through the hybrid, the target CTCs will be captured due to molecular recognition. The addition of benzonase nuclease leads to the cleavage of CTCs from the hybrid surface. During the course of cell capture and release, the ICR property will vary accordingly. The larger ionic current value with "on" state endows a sensitive capture, and detection of CTCs can be realized. The characterizations of the aptamer immobilization, the optimization of aptamer concentration, and the CTCs capture kinetics are detailed described in Supporting Information and Figures S8–10. The electrochemical assay was then adopted for the CCRF-CEM cell detection of various concentrations.

I−V curves with different concentrations of CCRF-CEM cells captured were recorded and are shown in Figure 5B. The ionic current at +1.0 V versus cell concentrations is displayed in Figure 5C. Owing to the increasing blockage effect by the captured cells, the currents decrease with cell concentration. In addition, as shown in the inset of Figure 5C, the current (I) is inversely proportional to the logarithm of cell concentrations from 300 to 1000 cells mL^{-1}. The calibration equation is I [μA] = $-0.063\log_{10}C + 0.26$ (where I is the current response at different cell concentrations. C is the concentration of CCRF-CEM cells in unit of cells/mL) with a correlation coefficient of 0.99. The detection limit is 80 cells mL^{-1}. Compared with other CTCs detection methods (Table S1 in the Supporting Information), the present method could reach a lower detection limit without the need for introducing any signal amplification strategy.

To evaluate the selectivity of this present platform, k562 cells and Raji cells were used as the other two types of cell models. With the same capture and detection processes as the CCRF-CEM cells, the electrical current signals were obtained. As shown in Figure 5D, only CCRF-CEM cells show a sharp drop of current, while k562 cells and Raji cells show slight changes. The reason is that only CCRF-CEM cell membranes possess a type of transmembrane receptor, which can recognize with the aptamer sgc8c,[44] thereby giving rise to the efficient and selective CCRF-CEM cell capture on the DAN/AAO surface. The captured cells cover the DAN/AAO hybrid surface, which efficiently blocks the ions transport through the hybrid, leading to varied I−V properties. The result confirms the excellent selectivity of the present method for cell capture and detection.

Finally, the successful release of CTCs from the DAN/AAO hybrid after cell capture is investigated. Benzonase nuclease was used to induce CCRF-CEM cell release.[26] To obtain the proper cell release time, the cells captured on the DAN/AAO hybrid were treated by enzyme solution (25 units mL^{-1} where one unit is the enzyme amount that catalyzes the reaction of 1 nmol of substrate per minute) for 5, 10, 20, 30, 40, and 50 min, respectively. As shown in Figure 5E, with the enzyme incubation time from 0 to 40 min, the current signals first increase and then reach a plateau, which indicates that the captured CCRF-CEM cells have been nearly released completely. Moreover, the cell viability changes during the course of cell capture and release were investigated by the Acridine Orange/Propidium Iodide (AO/PI) assay. As shown in Figure 5F, almost 100% of the cells are alive after being captured on the DAN/AAO hybrid. After release, there are no cells on the DAN/AAO hybrid (inset in Figure 5F). The released CCRF-CEM cells from the DAN/AAO hybrid were collected, and their viability was investigated. The fluorescent images in Figure S11 demonstrate that the benzonase nuclease enzyme shows slight damage to the cells. To investigate the performance of the present platform in a complex real blood sample, CCRF-CEM cells were added in the prepared volunteer blood solution at concentrations of 300, 500, 700, and 1000 cells mL^{-1}. The results are displayed in Figure 5G. A trend similar to that of the PBS solution is observed, verifying the practical application of the CCRF-CEM cell sensor in complex blood samples. The fact that most of the cells captured on DAN/AAO stay alive provide means for multimodal study, for example, by SERS and electrochemistry.

The durability of the prepared hybrid device is a critical factor toward practical bioanalysis. We have repeatedly used

one hybrid for CTC capture and detection after cell release. The very similar $I{-}V$ curves and ICR properties (Figure S12) in a continuous 5 day test demonstrate the excellent stability and reusability of the present hybrid toward CTCs capture, detection, and release.

In conclusion, we have demonstrated an engineered heterogeneous hybrid by chemically assembling DAN onto the top of AAO nanochannels. Due to the high surface-to-volume ratio of the AuNPs and high density of binding sites of PAMAM, the network formed has more surface area and can expose more functional groups, which results in more asymmetries in the structure and surface charge density of the DAN/AAO hybrid, thus leading to obvious rectified ion transport. The presence of amino groups on the DAN/AAO hybrid surface enables the anion-selective hybrid membrane to process ionic rectification and also promotes anion selectivity. Moreover, the ionic rectification properties can be tuned by ion valence and pH of the bulk solution. Under optimal conditions, highly sensitive circulating tumor cell detection based on this heterogeneous structure was successfully achieved with a detection limit of 80 cells mL^{-1}. This device also provides a sensitive multimodal (chemical, electrical, and optical) platform to study cell adhesion and cell behavior *in situ*.

■ ASSOCIATED CONTENT

Ⓢ Supporting Information

The Supporting Information is available free of charge at https://pubs.acs.org/doi/10.1021/acs.nanolett.9b05066.

> Materials and reagents, instrumentation, and experimental methods; contact angle of the DAN/AAO hybrid; SEM image of the DAN/AAO hybrid and corresponding EDS elemental mappings; TEM image of the DAN film; $I{-}V$ curve of the DAN/AAO hybrid with varied AuNPs concentrations; effect of the channel size and thickness of AAO; effect of temperature; XPS spectra of the thiol sgc8c-modified DAN/AAO hybrid; $I{-}V$ properties of the sgc8c-modified DAN/AAO hybrid; fluorescence images of the captured cells on the hybrid substrate; $I{-}V$ properties of the DAN/AAO hybrid with different incubation times; the current value at +1.0 V with different incubation times; fluorescence microscope images of cells with different incubation times; fluorescence microscope images of CCRF-CEM cells after releasing; the $I{-}V$ curves before and after CTCs release; the ionic current values at +1.0 V after varied cycles; comparison of different analytical methods for CCRF-CEM detection (PDF)

■ AUTHOR INFORMATION

Corresponding Authors

Chen Wang − *Department of Chemistry, School of Science, China Pharmaceutical University, Nanjing 211198, China; State Key Laboratory of Analytical Chemistry for Life Science, School of Chemistry and Chemical Engineering, Nanjing University, Nanjing 210023, China;* ⓞ orcid.org/0000-0001-6544-4065; Email: wangchen@cpu.edu.cn

Xing-Hua Xia − *State Key Laboratory of Analytical Chemistry for Life Science, School of Chemistry and Chemical Engineering, Nanjing University, Nanjing 210023, China;* ⓞ orcid.org/0000-0001-9831-4048; Email: xhxia@nju.edu.cn

Ju Li − *Department of Nuclear Science and Engineering and Department of Materials Science and Engineering, Massachusetts Institute of Technology, Cambridge, Massachusetts 02139, United States;* ⓞ orcid.org/0000-0002-7841-8058; Email: liju@mit.edu

Authors

Xiao-Ping Zhao − *Department of Chemistry, School of Science, China Pharmaceutical University, Nanjing 211198, China*

Fei-Fei Liu − *Department of Chemistry, School of Science, China Pharmaceutical University, Nanjing 211198, China*

Yuming Chen − *Department of Nuclear Science and Engineering and Department of Materials Science and Engineering, Massachusetts Institute of Technology, Cambridge, Massachusetts 02139, United States*

Complete contact information is available at:
https://pubs.acs.org/10.1021/acs.nanolett.9b05066

Author Contributions

J.L., X.H.X., and C.W. designed the experiments. C.W., X.P.Z., F.F.L., and Y. M. C. performed the experiments and wrote the paper. J.L. and X.H.X. revised the paper. All authors contributed to discussions.

Notes

The authors declare no competing financial interest.

■ ACKNOWLEDGMENTS

■ ABBREVIATIONS

DAN, dendrimer-Au nanoparticle network; AAO, anodic aluminum oxide; ICR, ionic current rectification; CTCs, circulating tumor cells; AuNPs, gold nanoparticles; PAMAM, dendrimer poly(amidoamine); CS$_2$, carbon disulfide; APTES, (3-aminopropyl) triethoxysilane; DMAP, 4-dimethylaminopyridine; f, ICR ratio; f_{max}, local maximum ICR ratio

■ REFERENCES

(1) Smith, P. L.; Baukrowitz, T.; Yellen, G. The inward rectification mechanism of the HERG cardiac potassium channel. *Nature* **1996**, *379* (6568), 833−836.

(2) Siwy, Z. S.; Howorka, S. Engineered voltage-responsive nanopores. *Chem. Soc. Rev.* **2010**, *39* (3), 1115−1132.

(3) Lan, W. J.; Edwards, M. A.; Luo, L.; Perera, R. T.; Wu, X.; Martin, C. R.; White, H. S. Voltage-rectified current and fluid flow in conical nanopores. *Acc. Chem. Res.* **2016**, *49* (11), 2605−2613.

(4) Jiang, Y. N.; Feng, Y. P.; Su, J. J.; Nie, J. X.; Cao, L. X.; Mao, L. Q.; Jiang, L.; Guo, W. On the origin of ionic rectification in DNA-stuffed nanopores: the breaking and retrieving symmetry. *J. Am. Chem. Soc.* **2017**, *139* (51), 18739−18746.

(5) Wang, C.; Xu, J. J.; Chen, H. Y.; Xia, X. H. Mass transport in nanofluidic devices. *Sci. China: Chem.* **2012**, *55* (4), 453−468.

(6) Zhang, Z.; Wen, L.; Jiang, L. Bioinspired smart asymmetric nanochannel membranes. *Chem. Soc. Rev.* **2018**, *47* (2), 322−356.

(7) Powell, M. R.; Cleary, L.; Davenport, M.; Shea, K. J.; Siwy, Z. S. Electric-field induced wetting and dewetting in single hydrophobic nanopores. *Nat. Nanotechnol.* **2011**, *6* (12), 798−802.

(8) Sun, Y.; Chen, S.; Chen, X.; Xu, Y.; Zhang, S.; Ouyang, Q.; Yang, G.; Li, H. A Highly selective and recyclable NO-responsive

nanochannel based on a spiroring opening- closing reaction strategy. *Nat. Commun.* **2019**, *10* (1), 1323.

(9) Perez-Mitta, G.; Peinetti, A. S.; Cortez, M. L.; Toimil-Molares, M. E.; Trautmann, C.; Azzaroni, O. Highly sensitive biosensing with solid-state nanopores displaying enzymatically reconfigurable rectification properties. *Nano Lett.* **2018**, *18*, 3303−3310.

(10) Li, C. Y.; Ma, F. X.; Wu, Z. Q.; Gao, H. L.; Shao, W. T.; Wang, K.; Xia, X. H. Solution-pH-modulated rectification of ionic current in highly ordered nanochannel arrays patterned with chemical functional groups at designed positions. *Adv. Funct. Mater.* **2013**, *23* (31), 3836−3844.

(11) Vlassiouk, I.; Siwy, Z. S. Nanofluidic diode. *Nano Lett.* **2007**, *7* (3), 552−556.

(12) Zhang, Z.; Li, P.; Kong, X.-Y.; Xie, G.; Qian, Y.; Wang, Z.; Tian, Y.; Wen, L.; Jiang, L. Bioinspired heterogeneous ion pump membranes: unidirectional selective pumping and controllable gating properties stemming from asymmetric ionic group distribution. *J. Am. Chem. Soc.* **2018**, *140* (3), 1083−1090.

(13) Zhang, Z.; Sui, X.; Li, P.; Xie, G.; Kong, X. Y.; Xiao, K.; Gao, L.; Wen, L.; Jiang, L. Ultrathin and ion-selective Janus membranes for high-performance osmotic energy conversion. *J. Am. Chem. Soc.* **2017**, *139* (26), 8905−8914.

(14) Cheng, L. J.; Guo, L. J. Ionic current rectification, breakdown, and switching in heterogeneous oxide nanofluidic devices. *ACS Nano* **2009**, *3* (3), 575−584.

(15) Wang, M.; Meng, H. Q.; Wang, D.; Yin, Y. J.; Stroeve, P.; Zhang, Y. M.; Sheng, Z. Z.; Chen, B. Y.; Zhan, K.; Hou, X. Dynamic curvature nanochannel-based membrane with anomalous ionic transport behaviors and reversible rectification switch. *Adv. Mater.* **2019**, *31* (11), 1805130.

(16) Zhang, Z.; Kong, X.-Y.; Xiao, K.; Liu, Q.; Xie, G.; Li, P.; Ma, J.; Tian, Y.; Wen, L.; Jiang, L. Engineered asymmetric heterogeneous membrane: a concentration-gradient-driven energy harvesting device. *J. Am. Chem. Soc.* **2015**, *137* (46), 14765−14772.

(17) Coglitore, D.; Merenda, A.; Giamblanco, N.; Dumee, L. F.; Janot, J.-M.; Balme, S. Metal alloy solid-state nanopores for single nanoparticle detection. *Phys. Chem. Chem. Phys.* **2018**, *20* (18), 12799−12807.

(18) Balme, S.; Lepoitevin, M.; Dumee, L. F.; Bechelany, M.; Janot, J.-M. Diffusion dynamics of latex nanoparticles coated with ssDNA across a single nanopore. *Soft Matter* **2017**, *13* (2), 496−502.

(19) Yanagi, I.; Akahori, R.; Takeda, K. Stable fabrication of a large nanopore by controlled dielectric breakdown in a high-pH solution for the detection of various-sized molecules. *Sci. Rep.* **2019**, *9*, 13143.

(20) Plett, T. S.; Cai, W. J.; Thai, M. L.; Vlassiouk, I. V.; Penner, R. M.; Siwy, Z. S. Solid-state ionic diodes demonstrated in conical nanopores. *J. Phys. Chem. C* **2017**, *121* (11), 6170−6176.

(21) Maglia, G.; Heron, A. J.; Hwang, W. L.; Holden, M. A.; Mikhailova, E.; Li, Q. H.; Cheley, S.; Bayley, H. Droplet networks with incorporated protein diodes show collective properties. *Nat. Nanotechnol.* **2009**, *4* (7), 437−440.

(22) Bolognesi, G.; Friddin, M. S.; Salehi-Reyhani, A.; Barlow, N. E.; Brooks, N. J.; Ces, O.; Elani, Y. Sculpting and fusing biomimetic vesicle networks using optical tweezers. *Nat. Commun.* **2018**, *9* (1), 1882.

(23) Ouyang, W.; Han, J.; Wang, W. Nanofluidic Crystals: Nanofluidics in a close-packed nanoparticle array. *Lab Chip* **2017**, *17* (18), 3006−3025.

(24) Liu, H.; Jiang, Q.; Pang, J.; Jiang, Z.; Cao, J.; Ji, L.; Xia, X.; Wang, K. A multiparameter pH-sensitive nanodevice based on plasmonicnanopores. *Adv. Funct. Mater.* **2018**, *28* (1), 1703847.

(25) Yue, W. Q.; Tan, Z.; Li, X. P.; Liu, F. F.; Wang, C. Micro/nanofluidic technologies for efficient isolation and detection of circulating tumor cells. *TrAC, Trends Anal. Chem.* **2019**, *117*, 101−115.

(26) Cao, J.; Zhao, X. P.; Younis, M. R.; Li, Z. Q.; Xia, X. H.; Wang, C. Ultrasensitive capture, detection, and release of circulating tumor cells using a nanochannel-ionchannel hybrid coupled with electro-

chemical detection technique. *Anal. Chem.* **2017**, *89* (20), 10957−10964.

(27) Zong, C.; Xu, M. X.; Xu, L. J.; Wei, T.; Ma, X.; Zheng, X. S.; Hu, R.; Ren, B. Surface-enhanced raman spectroscopy for bioanalysis: reliability and challenge. *Chem. Rev.* **2018**, *118* (10), 4946−4980.

(28) Wang, C.; Nie, X. G.; Shi, Y.; Zhou, Y.; Xu, J. J.; Xia, X. H.; Chen, H. Y. Direct plasmon-accelerated electrochemical reaction on gold nanoparticles. *ACS Nano* **2017**, *11* (6), 5897−5905.

(29) Yuan, J. H.; He, F. Y.; Sun, D. C.; Xia, X. H. A Simple method for preparation of through-hole porous anodic alumina membrane. *Chem. Mater.* **2004**, *16* (10), 1841−1844.

(30) Gittins, D. I.; Caruso, F. Spontaneous phase transfer of nanoparticulate metals from organic to aqueous media. *Angew. Chem., Int. Ed.* **2001**, *40* (16), 3001−3004.

(31) Gong, Y.; Yan, S. F.; Xia, P. F.; Wang, R. F.; Zhang, K. X.; Cui, L.; Yin, J. B. Porous microspheres based on hydroxyapatite-graft-poly (c-benzyl-L-glutamate) with improving homogeneity of hydroxyapatite and osteogenesis. *Mater. Lett.* **2019**, *250*, 206−209.

(32) Park, M. H.; Ofir, Y.; Samanta, B.; Rotello, V. M. Robust and Responsive dendrimer-gold nanoparticle nanocomposites via dithiocarbamate crosslinking. *Adv. Mater.* **2009**, *21* (22), 2323−2327.

(33) Wang, C.; Liu, F. F.; Tan, Z.; Chen, Y. M.; Hu, W. C.; Xia, X. H. Fabrication of bio-inspired 2D MOFs/PAA hybrid membrane for asymmetric ion transport. *Adv. Funct. Mater.* **2019**, 1908804.

(34) Ilaiyaraja, P.; Deb, A. K. S.; Ponraju, D. Removal of uranium and thorium from aqueous solution by ultrafiltration (UF) and PAMAM dendrimer assisted ultrafiltration (DAUF). *J. Radioanal. Nucl. Chem.* **2015**, *303* (1), 441−450.

(35) Yang, Z.; Shi, D.; Zhang, X.; Liu, H.; Chen, M.; Liu, S. Co-deposition motif for constructing inverse opal photonic crystals with pH sensing. *RSC Adv.* **2015**, *5* (85), 69263−69267.

(36) Zhang, Z.; Xie, G. H.; Xiao, K.; Kong, X. Y.; Li, P.; Tian, Y.; Wen, L. P.; Jiang, L. Asymmetric multifunctional heterogeneous membranes for pH- and temperature-cooperative smart ion transport modulation. *Adv. Mater.* **2016**, *28* (43), 9613−9619.

(37) Hsu, J. P.; Chen, Y. M.; Yang, S. T.; Lin, C. Y.; Tseng, S. Influence of salt valence on the rectification behavior of nanochannels. *J. Colloid Interface Sci.* **2018**, *531*, 483−492.

(38) Daiguji, H. Ion transport in nanofluidic channels. *Chem. Soc. Rev.* **2010**, *39* (3), 901−911.

(39) Rao, S.; Si, K. J.; Yap, L. W.; Xiang, Y.; Cheng, W. Free-standing bilayered nanoparticle superlatticenanosheets with asymmetric ionic transport behaviors. *ACS Nano* **2015**, *9* (11), 11218−11224.

(40) Pérez-Mitta, G.; Albesa, A. G.; ToimilMolares, M. E.; Trautmann, C.; Azzaroni, O. The influence of divalent anions on the rectification properties of nanofluidic diodes: insights from experiments and theoretical simulations. *ChemPhysChem* **2016**, *17* (17), 2718−2725.

(41) Wei, J.; Du, G.; Guo, J.; Li, Y.; Liu, W.; Yao, H.; Zhao, J.; Wu, R.; Chen, H.; Ponomarov, A. The rectification of mono-and bivalent ions in single conical nanopores. *Nucl. Instrum. Methods Phys. Res., Sect. B* **2017**, *404*, 219−223.

(42) Jani, A. M. M.; Losic, D.; Voelcker, N. H. Nanoporous anodic aluminium oxide: Advances in surface engineering and emerging applications. *Prog. Mater. Sci.* **2013**, *58* (5), 636−704.

(43) Wang, S. S.; Zhao, X. P.; Liu, F. F.; Younis, M. R.; Xia, X. H.; Wang, C. Direct plasmon-enhanced electrochemistry for enabling ultrasensitive and label-free detection of circulating tumor cells in blood. *Anal. Chem.* **2019**, *91*, 4413−4420.

(44) Pang, X. H.; Cui, C.; Su, M. H.; Wang, Y. G.; Wei, Q.; Tan, W. H. Construction of self-powered cytosensing device based on ZnOnanodisks@ g-C3N4 quantum dots and application in the detection of CCRF-CEM cells. *Nano Energy* **2018**, *46*, 101−109.

Supporting Information

Dendrimer-Au Nanoparticles Network Covered Alumina Membrane for Ion Rectification and Enhanced Bioanalysis

Chen Wang[1,2]*, Xiao-Ping Zhao[1], Fei-Fei Liu[1], Yuming Chen[3], Xing-Hua Xia[2]*, Ju Li[3]*

[1]Department of Chemistry, School of Science, China Pharmaceutical University, Nanjing, 211198, China

[2]State Key Laboratory of Analytical Chemistry for Life Science, School of Chemistry and Chemical Engineering, Nanjing University, Nanjing 210023, China

[3]Department of Nuclear Science and Engineering and Department of Materials Science and Engineering, Massachusetts Institute of Technology, Cambridge, MA 02139, USA

*To whom correspondence should be addressed. E-mail: liju@mit.edu;

xhxia@nju.edu.cn; wangchen@cpu.edu.cn

Materials and reagents. (3-aminopropyl) triethoxysilane (APTES) was purchased from Alfa Aesar. Aptamer sgc8c sequence: 5'-ATC TAA CTG CTG CGC CGC CGG GAA AAT ACT GTA CGG TTA GAT TTT TTT TTT-3'-$(CH_2)_6$-SH was ordered from Shanghai Shengong Biotechnology Co., Ltd. Acridine orange (AO), propidium iodide (PI) and RPMI-1640 culture medium were purchased from Nanjing KeyGen Biotech Co., Ltd. (Nanjing, China). Poly(amidoamine) (PAMAM, G_4 generation was used in this work), 6-mercapto-1-hexanol (MCH) and 4-dimethylaminopyridine (DMAP) were from Sigma-Aldrich. Carbon disulfide (CS_2) was purchased from Shanghai Macklin Biochemical Co., Ltd. Methanol was purchased from Cinc High Purity Solvents (Shanghai) Co., Ltd. Fetal bovine serum (FBS) and penicillin-streptomycin solution were purchased from Corning Co., Ltd. (Manassas). Benzonase nuclease was from EMD Millipore (USA). CCRF-CEM (CCL-119, T cell line, human, acute lymphoblastic leukemia, ALL) was obtained from Shanghai Institutes for Biological Sciences (China). The k562 (CCL-243, human CML) and the Raji (CCL-86, B lymphocyte, homosapiens, human) cells were obtained from Beijing Xiehe Hospital. Potassium hydroxide and hydrogen peroxide (30% H_2O_2) were purchased from Nanjing Chemical Reagent Co., Ltd. Phosphoric acid(H_3PO_4) and Tin(II) chloride were from Sinopharm Chemical Reagent Co., Ltd. Oxalic acid dehydrate, acetone, chromic acid (H_2CrO_4), chloroform and potassium chloride (KCL) were purchased from Shanghai Ling Feng Chemical Reagent Co., Ltd. Silica gel films were purchased from Shanghai Zhang's silicone rubber products Co., Ltd. Gold chloride ($HAuCl_4 \cdot 4H_2O$) was purchased from the First Reagent Factory (Shanghai, China). All reagents were of analytical grade. All solutions were prepared using ultrapure water (18.2 M Ω·cm) from the Millipore Elix 5 Pure Water System (Purelab Classic Corp., USA).

Instrumentation. The morphology of the prepared plasmonic gold-nanochannel hybrid structure and the captured cells was characterized using a scanning electron microscope (SEM, S-4800, Japan). The gold nanoparticles were characterized using transmission electron microscopy (TEM, JEM-2100, Japan). The presence of APTES was characterized by an X-ray photoelectron spectroscopy (XPS, K-Alpha, Thermo

Fisher Scientific, USA). UV-vis absorbance was recorded on a UV-1800 spectrophotometer. Surface contact angle measurements were conducted on an OCA 30 contact-angle system (Data Physics, Germany) at room temperature. Zeta potentials were measured by Malvern Zetasizer ZS90. The electrochemical detection was performed in 1 mM KCl solution on an electrochemical workstation (CHI 660E, Chenhua, China) with two Ag/AgCl electrodes as the anode and cathode. The captured cells on the DNPN/PAA hybrid were observed using confocal laser scanning microscope (CLSM, LSM800, Zeiss, Germany).

Experimental methods

Fabrication of DAN/AAO hybrid. AAO were prepared using the method described previously.[S1] A voltage of 40 V was used to anodically oxidize a high pure aluminum sheet in 0.3 M oxalic acid aqueous solution at 25 ^{o}C for 30 min. Subsequently, phosphate acid (5% wt) and chromic acid (1.5% wt) mixed solution was adopted to remove the resulting alumina membrane at 60 ^{o}C for 40 min, giving rise to a rough concave substrate. Then, the second anodic oxidation process was performed with the same condition as the first oxidized step for 4h. Afterwards, the aluminum substrate was removed by Tin(II) chloride solution followed by 5 % phosphate acid aqueous solution, and the barrier layer was detached. A well-ordered AAO was formed. For fabrication of DAN/AAO hybrid, 4-dimethylaminopyridine (DMAP) stabilized gold nanoparticles (AuNPs ~7 nm) was prepared using the method reported previously.[S2] Then, the AAO was immersed into 1% (3-aminopropyl) triethoxysilane (APTES) diluted in 2 mL ethanol solution for 12 h to obtain the amine-functionalized AAO, followed by rinsing with ethanol and dried by nitrogen gas. The prepared amine-functionalized AAO was then placed at the bottom of a small vial containing a 1.5 mL mixture consisting of 500 μL of 30 mM AuNPs aqueous solution, 500 μL of a 163 mM CS_2 methanol solution, and 500 μL of a 50 μM PAMAM dendrimer methanol solution. The gold nanoparticles were assembled on the top surface of AAO linked by CS_2, forming a gold nanoparticle network film. Following completion of the reaction, the remaining solution removed, DAN/AAO hybrid was then obtained. The zeta potential

of self-assembled DAN fragments was measured by Malvern Zetasizer ZS90, by mixing 500 µL of 0.6 mM AuNPs aqueous solution, 500 µL of a 163 mM CS_2 methanol solution, and 500 µL of a 50 µM PAMAM dendrimer methanol solution in 1.5ml KCl solutions with different pH varying from 3 to 11, for 10 min. These solutions (without AAO) showed turbidity (Tyndall effect) rapidly, indicating self-assembly into DAN fragments.
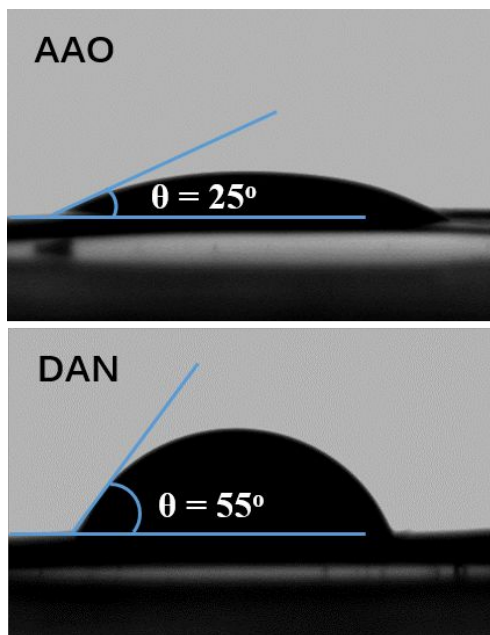
Measurement of the contact angle. Surface contact angle measurements were conducted on an OCA 30 contact-angle system (Data Physics, Germany) at room temperature. A drop of water was dipped on both side of DAN/AAO hybrid, then the contact-angle values observed be achieved from the images.

Immobilization of aptamer on DAN/AAO hybrid. The DAN/AAO hybrid structure was placed in the center of two 2 mL homemade half cells for surface modification and electrochemical detection. First, 100 µL of sgc8c aptamer solution (10 µM) was dropped onto the plasmonic gold film side at 4 °C for 6 h. After that, the excess solution was rinsed with PBS (pH 7.4) and then 100 µL 6-mercapto-1-hexanol (MCH,100 nM) was added in to the plasmonic gold film side for 1h to prevent nonspecific adsorption and control the spatial and orientation distribution of aptamer. Complete rinsing by deionized water was performed after each modification step.

Cell capture and release measurements. Cells were first cultured in flasks with RPMI-1640 medium at 37 °C under 5% CO_2 in the cell incubator followed by centrifuging at 600 rpm for 5 min, and then re-dispersed in PBS (10 mM, pH 7.4) with a density of 1×10^6 cells mL^{-1}. A 100 µL of CCRF-CEM cells suspension was dropped on the side of the DAN film of hybrid and then incubated in incubator. After cells capture, the DAN/AAO hybrid was washed by PBS buffer to remove the nonspecifically adsorbed cells. A 200 µL benzonase nuclease (25 units mL^{-1}, EMD Millipore) was used to release the CCRF-CEM cells from the hybrid structure for 5, 10, 20, 30, 40, 50 min, respectively. The electrochemical measurement was used to record the signal response from -1.0 V to +1.0 V by an electrochemical workstation (CHI 660E, Chenhua, China) with two Ag/AgCl electrodes with a scanning rate of 50 mV/s. Subsequently, cell viability of the captured and released cells was determined by 1 µg

mL^{-1} acridine orange (AO) and 1 μg mL^{-1} propidium iodide (PI) mixture solution after cells capture on the DAN/AAO hybrid. After the cells were released, the collected cells solution was also used to AO/PI staining assay experiment. Via AO/PI staining method, the dead and live cells were observed under a fluorescence inversion microscope system (Nikon, TI-U) and confocal laser scanning microscope (CLSM, LSM800, Zeiss, Germany).

Blood sample preparation. For blood sample detection, 300, 500, 700 and 1000 cells mL^{-1} CCRF-CEM cells were added into the prepared blood sample that was collected from healthy volunteers. After being centrifuged at 1500 rpm for 5 min and scrapped supernatant of the above sample, 100 μL sediment of buffer was added onto the DAN film, incubated for 60 min in the cell incubator. Finally, PBS solution was used to wash the DAN/AAO hybrid, and then the *I-V* profiles of the DAN/AAO hybrid from -1.0 V to +1.0 V were recorded.

Figure S1. Contact angle of the DAN/AAO hybrid. The upper one is from AAO layer, and the bottom is from DAN film. The data were measured by the contact angle meter (Goniometer).
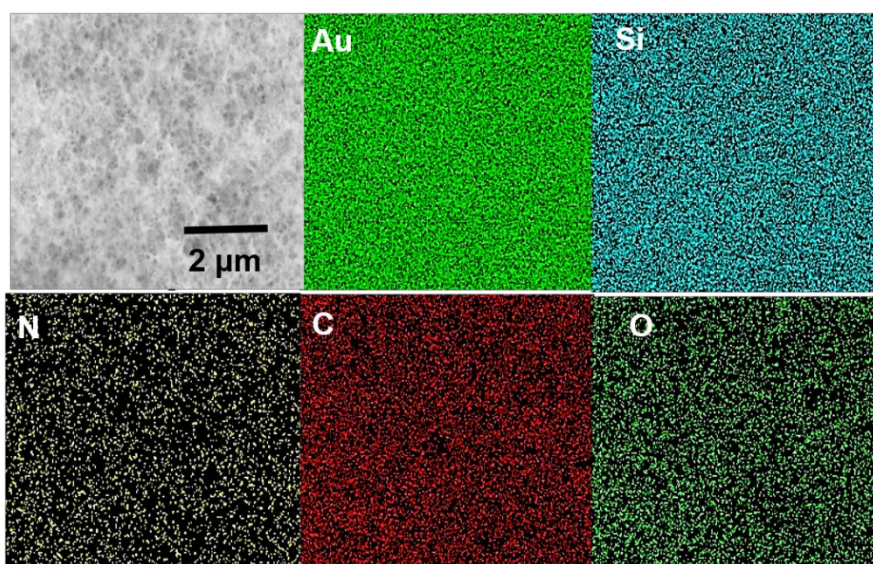
Figure S2. SEM image of the DAN/AAO hybrid and corresponding EDS elemental mappings of Au, Si, N, C and O. The scale bar is 2 μm.
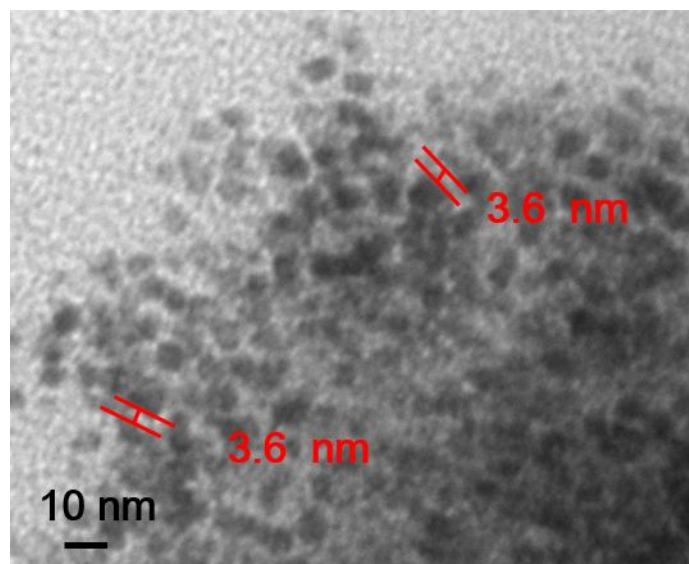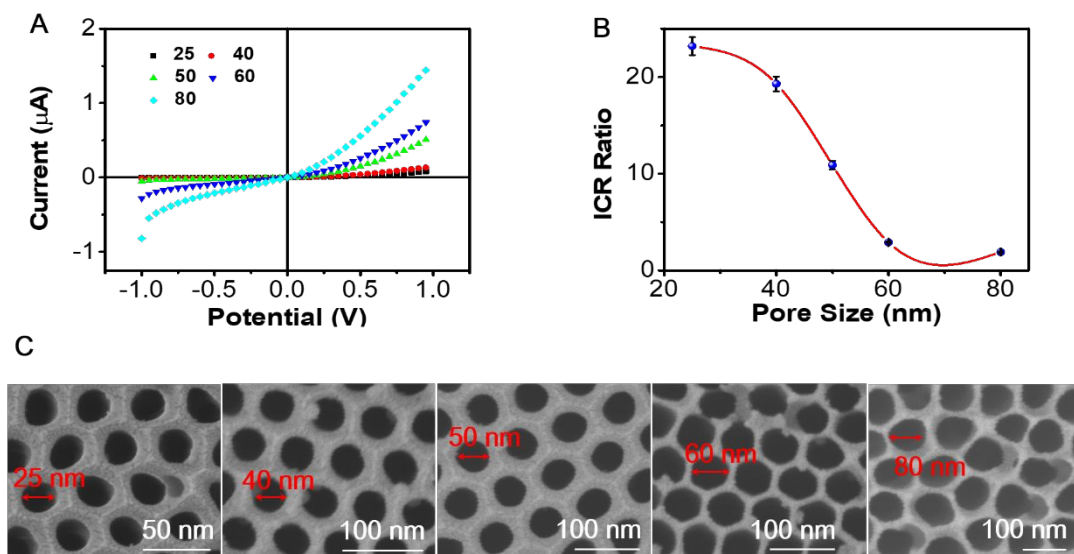
Figure S3. TEM image of the DAN film. AuNPs, PAMAM and CS$_2$ were assembled in solution to form the same structure of DAN film.
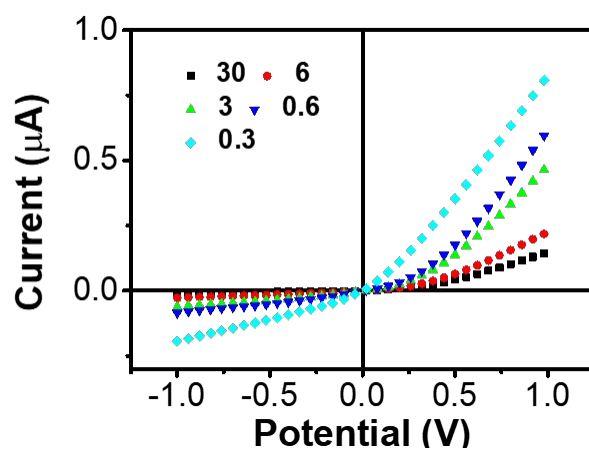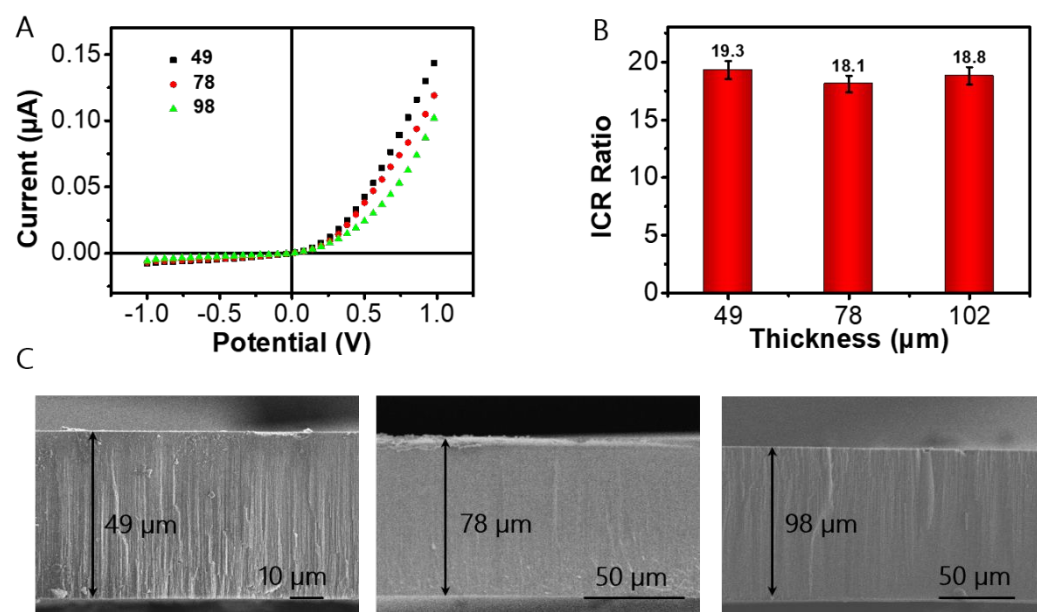

Figure S4. *I-V* curve of DAN/AAO hybrid with varied AuNPs concentrations (30 mM, 6 mM, 3 mM, 0.6 mM, 0.3 mM).
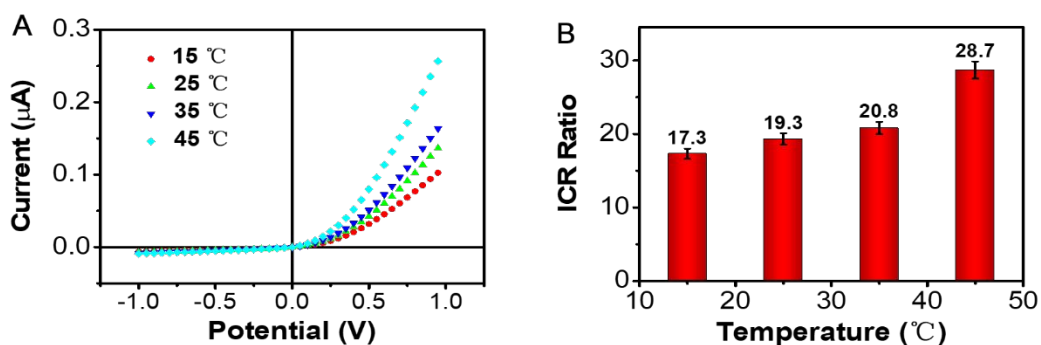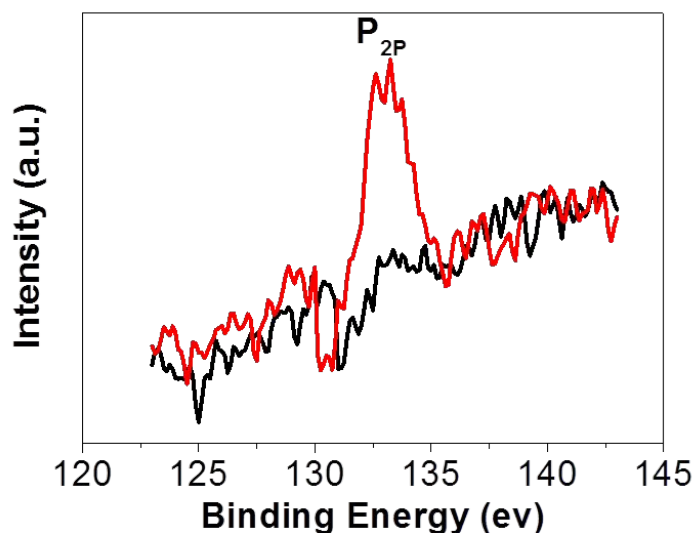
Figure S5. Effect of channel size of AAO on the *I-V* curves and ICR ratio.

Figure S6. Effect of AAO thickness on the *I-V* curves and ICR ratio. (A) *I-V* curves of the hybrid with varied AAO thickness (49, 78, 98 μm). (B) ICR ratio of the hybrid with varied AAO thickness (49, 78, 98 μm). (C) SEM images of AAO with different thickness.

Figure S7. Effect of temperature on the *I-V* curves and ICR ratio.

Figure S8. XPS spectra of thiol sgc8c modified DNPN/PAA hybrid (red curve in was sgc8c modified DNPN/PAA hybrid; black curve was the pure PAA membrane).

Aptamer probe sgc8c was first bound to the side of DAN film by Au-S bond for CTCs capture and release (Figure 5A). As shown in Figure S8, an obvious P*2p* peak (red line) in the DAN/AAO hybrid from the P element in sgc8c can be observed but no signal for the pure DAN/AAO hybrid membrane (black line), demonstrating the efficient modification of sgc8c within DAN/AAO hybrid.
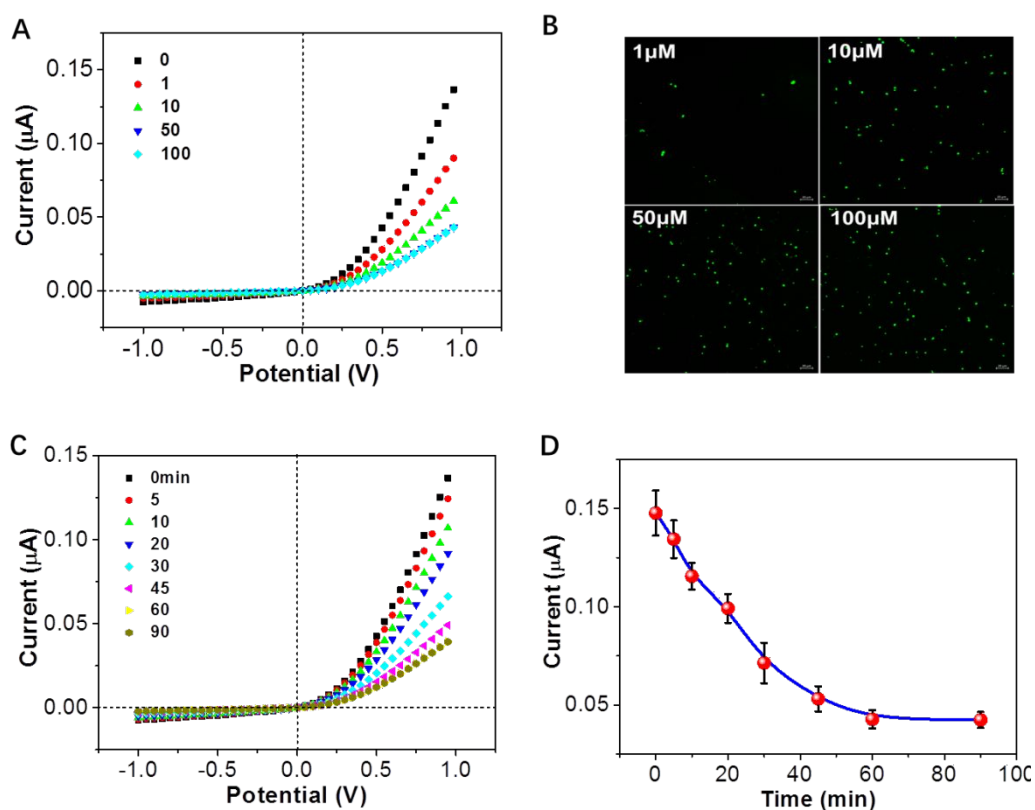
Figure S9. (A) *I-V* properties of different concentration of sgc8c modified hybrid membranes after capture cells: black curve, bare hybrid membrane; red curve, 1 μM sgc8c-modified hybrid; green curve, 10 μM sgc8c-modified hybrid; dark blue curve, 50 μM sgc8c-modified hybrid; light blue curve, 100 μM sgc8c-modified hybrid. (B) Fluorescence images of the captured cells on hybrid substrate modified with different concentrations of aptamer sgc8c (1, 10, 50 100 μM). Cell concentration: 1×10^6 cells mL^{-1}. (C) Effect of the CCRF-CEM cells incubation time on *I-V* properties of DNPN/PAA hybrid. (D) The current value at $+1$ V with different incubation times. The cell concentration is 1×10^6 cells mL^{-1}.

To realize efficient trap of CCRF-CEM cells, influence of the aptamer concentration was first examined (Figure S9A). It is found that increasing the aptamer concentration from 0 μM to 10 μM, the ionic current values at +1.0 V first declines sharply, and then reaches a plateau at 50 μM. To explain this phenomenon directly, the confocal laser scanning microscope images of cells onto the DAN/AAO hybrid stained by AO/PI assay were taken (Figure S9B). AO dye with green fluorescence can transport

through the cell membrane to bound with DNA, however, a red fluorescent dye PI only bind with DNA after cell membrane destroyed. From fluorescence images, with increased aptamer concentration, the amount of trapped cells on DAN/AAO increases until aptamer concentration reaches 50 μM. Thus, 50 μM was chosen as the aptamer concentration used in the following work. In addition, the optimum cell capture time also has a great importance to cell capture. As shown in Figure S9C, when cells solution added on the DAN film was incubated for different times (5, 10, 20, 30, 45, 60, and 90 min) at 37 °C, the *I-V* properties drop continuously in the first 45 min, and then reaches stable after 60 min. The ionic current value at + 1.0 V versus incubation time is shown in Figure S9D. The constant ionic current at + 1.0V indicates that the captured cells reach saturation after 60 min.
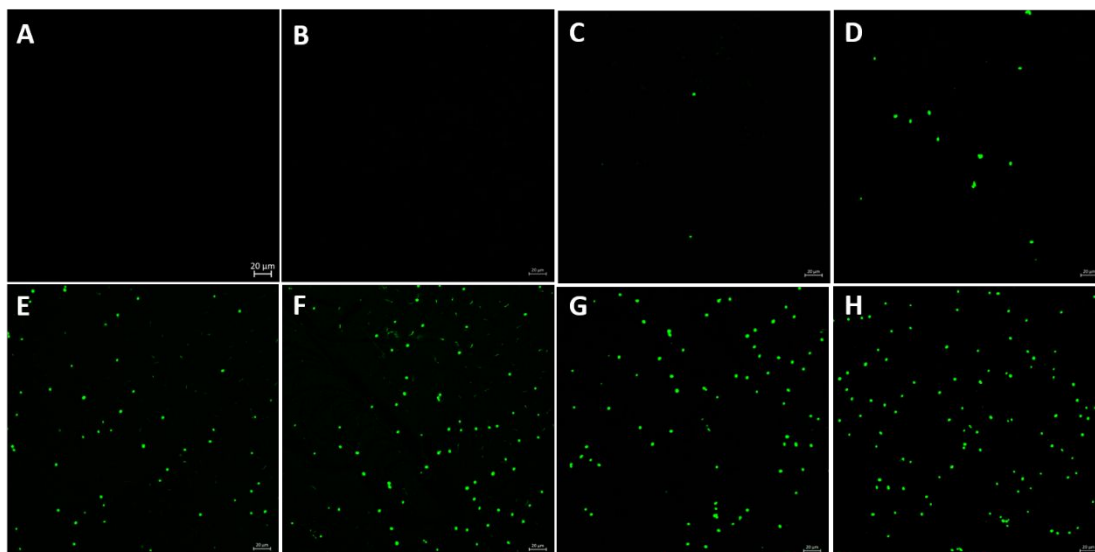
Figure S10. Fluorescence microscope images of CCRF-CEM cells after capture on DNPN/PAA hybrid with different incubation time.

The confocal laser scanning microscope was used to take the images after cell capture on the DAN/AAO hybrid with different time (Figure S10). It is seen that the captured cells number increases with increasing the capture time. When the capture reaches 60 min, the captured cells nearly cover the whole DAN/AAO surface, and there is no space to trap more cells.
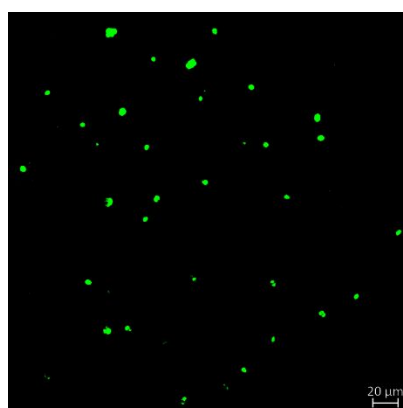
Figure S11. Fluorescence microscope images of CCRF-CEM cells after releasing from DNPN/PAA hybrid.
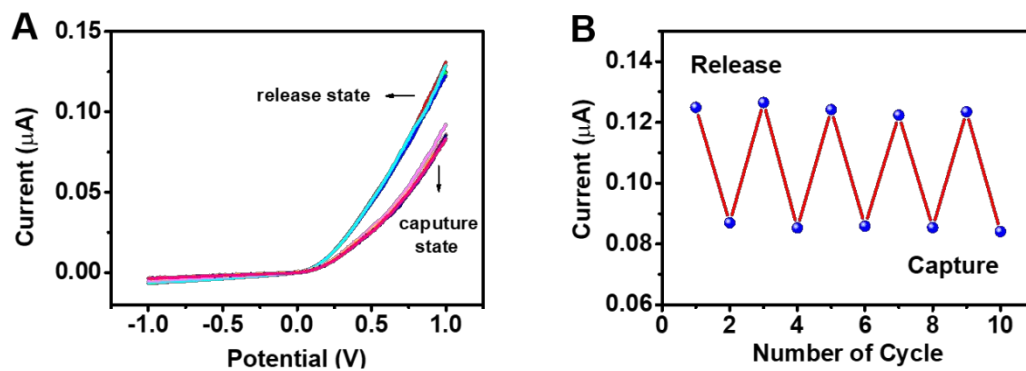
Figure S12. (A) The *I-V* curves before and after CTCs release (the captured CTCs is 300 cell mL^{-1}). (B) The ionic current values at 1.0 V from Figure S12A after varied cycles of cell capture and release.

Table S1. Comparison of Different Analytical method for CCRF-CEM detection

Cytosensor	Detection method	Linear range	Detection limit	Reference
HA-MNPs	QCM	8.0×10^3-1.0×10^5	8000	S3
aptamer/APBA-MWCNTs	EIS	1.0×10^3-1.0×10^7	1000	S4
aptamer/Ag NCs	Flow cytometry	7.5×10^3 -6.25×10^5	7500	S5
aptamer/PAA	LSV	1×10^2-1×10^6	100	S6
aptamer-microfluidic	Fluorescence	4×10^2-5.0×10^6	400	S7
aptamer/GO	Fluorescence	1×10^2-1×10^7	100	S8
ConA/ GQDs	EIS	5×10^2-1×10^5	246	S9
CdS/ ZnO nanorod arrays	ECL	300-10^4	256	S10
AAO	Interference spectroscopy	1000-100,000 cells/mL	<1000 cells/mL	S11
aptamer/DNPN/PAA	LSV	50-1×10^7	80	this work

HA MNPs: hyaluronic acid coated magnetic nanoparticles; APBA-MWCNTs: 3-aminophenylboronic acid-functionalized multiwalled carbon nanotubes; Ag NCs: silver nanoclusters; PAA: porous anodic alumina; GO: graphene oxide; GQDs: graphene quantum dots; ConA : Concovalin A ; QCM: quartz crystal microbalance; EIS: electrochemical impedance spectroscopy; ECL: electrochemiluminescence; AAO: anodic aluminium oxide; LSV: linear sweep voltammetry.

References

(S1) Yuan, J. H.; He, F. Y.; Sun, D. C.; Xia, X. H. A Simple method for preparation of through-hole porous anodic alumina membrane. *Chem. Mater.* **2004,** *16* (10), 1841-1844.

(S2) Gittins, D. I.; Caruso, F. Spontaneous phase transfer of nanoparticulate metals from organic to aqueous media. *Angew. Chem. Int. Edit.* **2001,** *40* (16), 3001-3004.

(S3) Zhou, Y.; Xie, Q. Hyaluronic acid coated magnetic nanoparticles based selective collection and detection of leukemia cells with quartz crystal microbalance. *Sens. Actuators, B* **2016,** *223,* 9-14.

(S4) Paredes Aguilera, R.; Romero Guzman, L.; Lopez Santiago, N.; Burbano Ceron,

L.; Camacho Del Monte, O.; Nieto Martinez, S. Flow cytometric analysis of cell surface and intracellular antigens in the diagnosis of acute leukemia. *Am. J. Hematol.* **2001,** *68* (2), 69-74.

(S5) Yin, J.; He, X.; Wang, K.; Xu, F.; Shangguan, J.; He, D.; Shi, H. Label Free and Turn on Aptamer Strategy for Cancer Cells Detection Based on a DNA Silver Nanocluster Fluorescence upon Recognition Induced Hybridization. *Anal. Chem.* **2013,** *85* (24), 12011-12019.

(S6) Cao, J.; Zhao, X. P.; Younis, M. R.; Li, Z. Q.; Xia, X. H.; Wang, C. Ultrasensitive Capture, Detection, and Release of Circulating Tumor Cells Using a Nanochannel Ion Channel Hybrid Coupled with Electrochemical Detection Technique. *Anal. Chem.* **2017,** *89* (20), 10957-10964.

(S7) Cao, L. L.; Cheng, L. W.; Zhang, Z. Y.; Wang, Y.; Zhang, X. X.; Chen, H.; Liu, B. H.; Zhang, S.; Kong, J. L. Visual and high throughput detection of cancer cells using a graphene oxide based FRET aptasensing microfluidic chip. *Lab. Chip.* **2012,** *12* (22), 4864-4869.

(S8) Tan, J.; Lai, Z.; Zhong, L.; Zhang, Z.; Zheng, R.; Su, J.; Huang, Y.; Huang, P.; Song, H.; Yang, N.; Zhou, S.; Zhao, Y. A Graphene Oxide Based Fluorescent Aptasensor for the Turn on Detection of CCRF CEM. *Nanoscale Res. Lett.* **2018,** *13* (1), 66.

(S9) Chowdhury, A. D.; Ganganboina, A. B.; Park, E. Y.; Doong, R. A. Impedimetric biosensor for detection of cancer cells employing carbohydrate targeting ability of Concanavalin A. *Biosens. Bioelectron.* **2018,** *122,* 95-103.

(S10) Liu, D.; Wang, L.; Ma, S.; Jiang, Z.; Yang, B.; Han, X.; Liu, S. A novel electrochemiluminescent immunosensor based on CdS-coated ZnO nanorod arrays for HepG2 cell detection. *Nanoscale*, **2015,** *7* (8), 3627-3633.

(S11) Kumeria, T.; Kurkuri, M. D.; Diener, K. R.; Parkinsona, L.; Losic, D. Label-free reflectometric interference microchip biosensor based on nanoporous alumina for detection of circulating tumour cells, *Biosens. Bioelectron.* **2012,** *35* (1), 167-173.